RSC Advances

PAPER

View Article Online
View Journal | View Issue

Check for updates

Cite this: *RSC Adv.*, 2017, 7, 44523

Facile fabrication of polyaniline@γ-MnOOH on a buckypaper ternary composite electrode for free-standing supercapacitors†

Lichen Xia,[a] Lujun Pan,*[a] Muhammad Asif,[b] Dongmei Zhang,[a] Muhammad Usman,[a] Shuaitao Yang,[a] Nan Zhou,[a] Yunping Hu[c] and Yuezhen Bin[c]

Received 31st July 2017
Accepted 4th September 2017

DOI: 10.1039/c7ra08431e

rsc.li/rsc-advances

Ternary composites as electrode materials have attracted extensive attention due to their excellent electrochemical performance in energy-storage technologies as compared to single or binary composites. Herein, we demonstrated a facile two-step method to construct a new hierarchical nanocomposite by combing buckypaper (BP) with γ-MnOOH nanorods and polyaniline. BP is used as a conductive substrate for the synthesis of free-standing hierarchical electrodes. The structural characterizations revealed the growth of a hierarchical porous structure of the ternary electrode. The synthesized polyaniline@γ-MnOOH–BP ternary composite electrode shows a maximum specific capacitance of 567.5 F g^{-1} at a current density of 0.5 A g^{-1} and a relatively high areal capacitance of 301.2 mF cm^{-2} at a current density of 0.27 mA cm^{-2}. This intriguing result is ascribed to the good combination of BP, γ-MnOOH, and PANI. We believe that this ternary composite electrode has potential in portable, environmentally friendly, and wearable applications for next generation energy-storage devices.

1. Introduction

With the rise of an ever-growing market of portable electronics and the automobile industry in recent few years, renewable and efficient energy-storage devices are urgently required. Supercapacitors (SCs) are typical devices for energy-storage systems due to their lower cost, higher power density and moderate energy density, faster charge/discharge process, longer cycle life, and environmental friendliness as compared to the other types of energy-storage devices such as Li-ion batteries. Recently, significant attention has been paid towards the development of thin film capacitors that are increasingly required for light and wearable micro-devices in many new emerging energy-storage fields. Carbon nanomaterials, such as graphene,[1–3] multiwalled carbon nanotubes (MWCNTs),[4–7] and carbon nanofibers (CNFs),[8] as a film electrode have been one of the most popular materials for SCs. Some groups have fabricated porous graphene papers[1] and MWCNT papers (buckypapers),[7] which show good electrochemical performance owing to the excellent properties, such as high conductivity, good stability, and outstanding mechanical properties, of the two kinds of nanomaterials.[9–11] Furthermore, carbon nanomaterials work as a film electrode directly without any binder, and this free-standing interconnected structure builds a conductive network due to the self-assembly effect and van der Waals forces.

Based on the advantages of carbon-based SCs, many pseudocapacitive materials were combined to obtain more electron storage[12] due to their multi-oxidation states for electron transfer and reversible adsorption. To date, many types of active materials (such as metal oxides/hydroxides and conductive polymers[13] *etc.*) have been used as alternatives for designing electrodes for SCs with high cycling stability and high energy/power density. Among them, manganese oxyhydroxide (MnOOH)[14,15] is abundant in natural storage with a stable trivalence under ambient conditions, which is a good candidate as an electrode material. Compared to MnO_2, MnOOH has an inherent redox reaction during the facile electron-transfer process and is the main electroactive species for charge storage/delivery in the redox transition of the corresponding manganese oxide.[16,17] Recently, Li *et al.*[18] reported that MnOOH nanorods, synthesized by the solvothermal method, showed a specific capacitance of 132 F g^{-1}; however, the poor electronic conductivity often hindered the electrode utilization for SCs. Sun *et al.*[15] fabricated the reduced graphene oxide@MnOOH (RGO@MnOOH) aerogel composite, which exhibited a higher specific capacitance of 327 F g^{-1}. Similarly, Zhang *et al.*[19] fabricated an α-MnOOH–CNT film electrode by an electrophoretic deposition process that showed a higher capacitance than

---

[a] *School of Physics, Dalian University of Technology, Dalian 116024, PR China. E-mail: lpan@dlut.edu.cn; Fax: +86 411 84709304*

[b] *Department of Materials Science and Engineering, College of Engineering, Peking University, Beijing 100871, China*

[c] *Department of Polymer Science and Engineering, Faculty of Chemical, Environmental and Biological Science and Technology, Dalian University of Technology, Dalian 116024, PR China*

† Electronic supplementary information (ESI) available. See DOI: 10.1039/c7ra08431e

the single MnOOH electrode, with the specific capacitance and areal capacitance of 327 F g^{-1} and 200 mF cm^{-2}, respectively. More recently, a ternary composite electrode exhibited higher capacitance than the binary composite electrode, which became a new research focus.[20] Among the pseudocapacitive materials, polyaniline (PANI), a conductive P-type conjugated polymer, has been studied as an active material[13] in the binary composite electrode. PANI is a kind of classical pseudocapacitive material, similar to some metal oxides. However, it is very hard to control the growth of PANI because of excessive agglomeration, which leads to a decrease in accessible surface areas and inferior ionic exchange.

This study was aimed at the fabrication of a new ternary-composite electrode that was combined with BP, γ-MnOOH, and PANI. In recent studies, many kinds of MnO_2 and PANI nanocomposites have been fabricated due to their good electrochemical performances.[21–25] However, there are less studies on the use of γ-MnOOH for supercapacitors; in this study, a γ-MnOOH nanorod array grown on the conductive BP was first fabricated by a reaction between $KMnO_4$ and SDS. Because of the nanorod array structure, the large surface area of γ-MnOOH is completely accessible to grow PANI. This new hierarchical structure not only ensures good electronic conductivity between BP and γ-MnOOH nanorods, but also restrains the agglomeration of PANI to boost the electrochemical performance. Moreover, the PANI nanosheets directly grown on the surface of MnOOH nanorods would supply more electronic paths. The interconnected porous structures would increase the accessible area and enhance the ability of the ion insertion/deinsertion process. The hierarchical ternary film of porous PANI nanosheets would exhibit higher specific capacitance and areal capacitance than those reported in a previous study.[19]

2. Material and methods

2.1. Preparation method of BP

For the synthesis of BP, 200 mg MWCNTs (Chengdu Organic Chemistry Co., LTD) were ground for half an hour and then dispersed in deionized water (500 ml) containing 1 wt% of surfactant X-100. A uniform dispersion was achieved by stirring MWCNTs in the sonication bath for 30 min. The dispersion was filtered through a cellulose membrane (0.45 μm) to form buckypapers, and the resulting filter cake was rinsed with deionized water to wash away the residual surfactant. Then, the filter cake was dried in an oven at 60 °C for 20 h and then peeled from the filter membrane.

2.2. Synthesis of the γ-MnOOH–BP (MBP) composite

γ-MnOOH coated on BP was synthesized using a simple hydrothermal method. Herein, 0.3 g of potassium permanganate ($KMnO_4$; Aladdin Reagent, AR) was added to 40 ml of 0.02 M sodium lauryl sulfate (SDS; Sinopharm Chemical Reagent, CP) solution, and the mixed solution was stirred for 30 min to fully disperse $KMnO_4$. Then, the obtained mixed solution and BP were transferred to a 50 ml Teflon-lined autoclave that was then maintained at 150 °C for 12 h under autogenous pressure. Upon cooling to room temperature, the γ-MnOOH–BP composite was obtained by washing with distilled water. Finally, the composite was dried at 60 °C for 12 h. Similarly, the single γ-MnOOH sample without BP was synthesized under the same condition.

2.3. Synthesis of PANI@γ-MnOOH–BP (PMBP) and PANI–BP (PBP) composites

In a typical procedure, 0.6 g of aniline monomer (Aladdin Reagent, AR) was dispersed in a 30 ml of 0.15 M camphor sulfonic acid (CSA; Aladdin Reagent, 99%) solution *via* sonication for 10 min.[26] Similarly, 1.8 g ammonium peroxydisulfate (APS; Aladdin Reagent, 99.99%) was added to 30 ml ultrapure water under continuous stirring for 10 min. Both kinds of solutions were mixed together for 1 min, and γ-MnOOH–BP and BP were, respectively, immersed in the mixed solution for 6 h at room temperature without stirring. Finally, the resultant products were rinsed with deionized water and dried at 60 °C for 6 h.

2.4. Characterization

The morphology and structure of the synthesized nanocomposites were analyzed by field emission scanning electron microscopy (FE-SEM, NOVA NanoSEM450), transmission electron microscopy (TEM; JEOL JEM-2100), Raman spectroscopy (Renishaw inVia plus, semiconductor laser, 532 nm), X-ray diffraction (XRD, Cu Kα radiation, PANalytical B.V. Empyrean), and X-ray photoelectron spectroscopy (XPS, VG ESCALAB 250Xi). Electrochemical performance was measured *via* a conventional three-electrode electrochemical workstation (Modulab CHI660E) using a platinum plate (20 × 20 mm^2) as the counter electrode and Ag/AgCl as the reference electrode in a 1 M Na_2SO_4 aqueous solution as an electrolyte. The loading of the ternary electrode is 9.2 mg, and the mass percentages of BP, γ-MnOOH, and PANI in the PMBP composite electrode are 51.1%, 16.3%, and 32.6%, respectively.

3. Results and discussion

3.1. Morphology and composition characterizations

The overall process for the fabrication of BP, MBP, and PMBP composites is illustrated in Fig. 1. The BP was first filtered through a vacuum pump; after the reaction by the hydrothermal method at 150 °C for 12 h, the as-obtained MBP composite became brown, and the cross-sectional view of MBP is shown in Fig. S1.† After the polymerization of the aniline monomer on MBP, the surface of the PMBP composite became dark green. The cross-sectional view of PMBP is shown in Fig. S2.†

Typical XRD patterns of the as-prepared BP, hierarchical MBP, and PMBP composites are shown in Fig. 2. The diffraction peak of pure BP at ~26° corresponds to the (002) plane of MWCNTs. After the hydrothermal process, the diffraction patterns of the MBP composite are perfectly indexed on the monoclinic unit cell for γ-MnOOH with the parameters a = 0.53 nm, b = 0.5278 nm, and c = 0.5307 nm (JPSDS, no. 41-1379).[27–29] Diffraction peaks of pure γ-MnOOH shown at 2θ = 26.1°, 33.9°, 35.5°, 37.2°, 40.4°, 41°, 51.7°, 53.7°, and 54.8° well

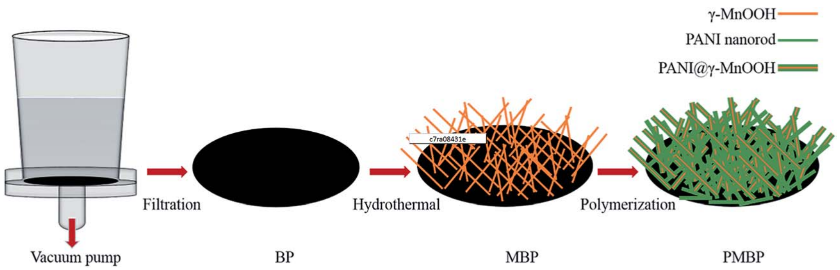

Fig. 1 Schematic for the fabrication of BP, MBP, and PMBP composites.

match the (11−1), (020), (111), (20−2), (210), (211), (22−2), and (11−3) planes. Based on the diffraction patterns of the ternary film PMBP composite, it can be concluded that the peaks at ∼20° and ∼26° (ref. 20) correspond to the planes of PANI, and the diffraction peak of γ-MnOOH was covered by PANI except for the most intense peak at 26.1°.

FE-SEM images in Fig. 3a and b show the BP and γ-MnOOH nanorod arrays growing on BP, which reveal that the carbon nanotubes and γ-MnOOH nanorods array are tightly interconnected. γ-MnOOH obtained by the hydrothermal method exhibits a rod-like morphology, and its length varies from 1 to 5 μm and the diameter varies from 20 to 200 nm. The as-synthesized novel nanostructures exhibit abundant void spaces that ensure that more aniline monomer is fully adsorbed on the surface of MWCNTs and γ-MnOOH nanorods. Fig. 3c shows some shorter but wider PANI nanorods growing on MBP, indicating that the aniline monomers have initiated the polymerization on the surface of γ-MnOOH or grown as PANI nanorods on BP. High-magnification image of PMBP is shown in Fig. S3.† There are many small PANI nanoparticles on the surface of these fibers. In addition, the rough surface of PANI supplies more positions for a sufficient electrochemical reaction between an electrode and electrolyte, which would have a contribution to enhance the electrochemical performance of the PBMP electrode. The EDS mapping images in Fig. 3d confirm the existence of C, Mn, N, and O elements in PMBP. Moreover, the uniform distribution of Mn and N elements indicates homogeneous growth of γ-MnOOH and PANI nanostructures on BP.

The morphology of active materials on BP was analyzed by TEM. Fig. 4a shows the TEM image of an individual γ-MnOOH nanorod and the inset shows its fast Fourier transform (FFT) pattern. The diffraction points from the FFT pattern are easily observable, indicating the crystalline nature of γ-MnOOH nanostructures. Fig. 4b shows the high-resolution TEM (HRTEM) image of the γ-MnOOH nanorod, and the inset shows the local enlarged image. In the magnified image, the lattice fringe of γ-MnOOH can be observed with an interplanar distance of 0.34 nm corresponding to the (11−1) plane.[27] PANI is coated on the surface of MBP; this results in the growth of PANI nanostructures around CNTs and γ-MnOOH, as indicated by the TEM image shown in Fig. 4c. The position 1 and position 2 show the structures of PANI@γ-MnOOH and PANI@CNTs, which indicate that conductive PANI acts as a bridge for effective electronic pathways between CNTs and the surface of γ-MnOOH. The HRTEM image of PMBP and the enlarged image of PMBP are displayed in Fig. 4d. The magnified image demonstrates the existence of amorphous PANI around the γ-MnOOH nanostructures. The interplanar distance of the γ-MnOOH lattice fringes was calculated to be 0.34 nm, which corresponded to the (11−1) plane.

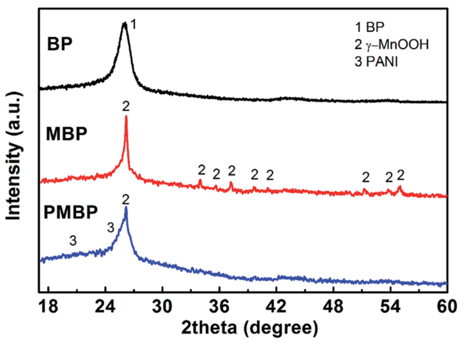

Fig. 2 XRD patterns of the BP, MBP, and PMBP composite.

For further analysis of the BP, MBP, and PMBP hierarchical composites, Raman spectroscopy was employed using a laser with an excitation wavelength of 532 nm. Fig. 5 depicts the existence of two prominent peaks around 1349 and 1579 cm^{-1} for BP, which are assigned to the D- and G-band, respectively. It can be observed that the peak corresponding to the G-band has a higher intensity than that of D-band; this reveals that the CNTs have good crystallinity and BP has good conductivity as an electrode.[30] The other six main peaks located at 334, 382, 526, 553, 617, and 643 cm^{-1} originate from the Mn–O vibrational modes of γ-MnOOH, corresponding with those reported by Bernard *et al.*[31] This demonstrates the formation of γ-MnOOH in the MBP binary composite. For the PMBP composite, the peaks at 1159 and 1213 cm^{-1} are related to the C–H bend of the quinoid ring and benzenoid ring, respectively. The peak at 1336 cm^{-1} is attributed to the C–N^{+} stretching vibration, and the peak at 1500 cm^{-1} is associated with the C=C stretching mode of the quinoid ring. The peaks corresponding to γ-MnOOH become weak and invisible; this indicates that the γ-MnOOH nanorods are covered by PANI.[32]

The chemical binding states of the as-prepared PMBP composite were analyzed by XPS, as shown in Fig. 6. Fig. 6a shows that the C 1s spectrum can be divided into three constituent peaks centered at 284.5 eV, 285.3 eV, and 286.5 eV,

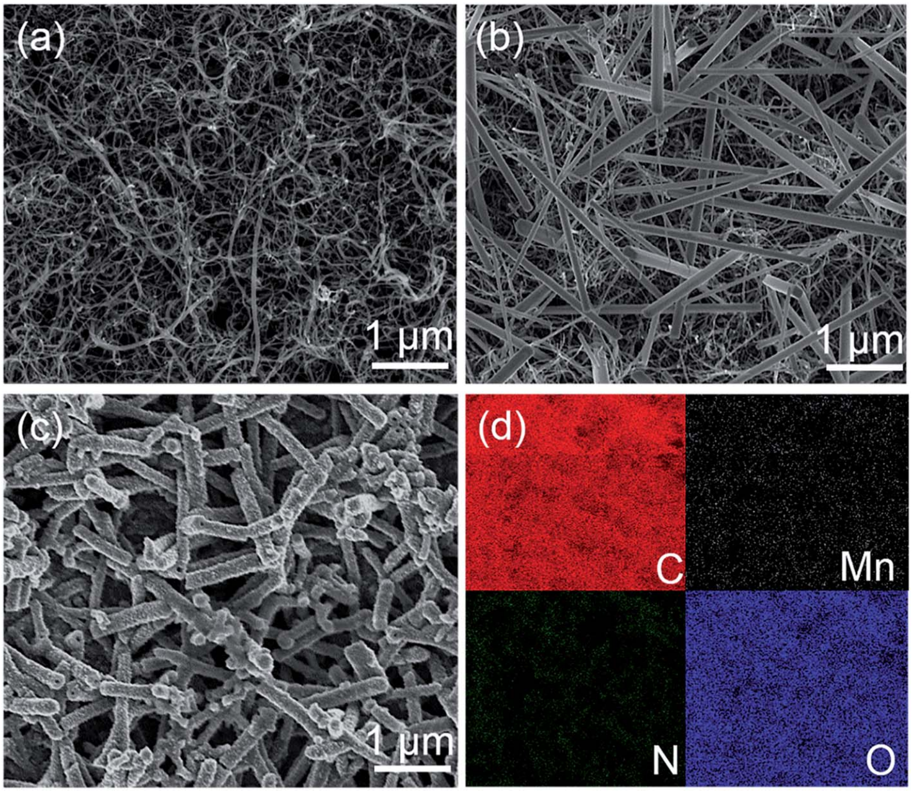

Fig. 3 FE-SEM images of (a) BP, (b) MBP, and (c) PMBP and corresponding (d) EDS mappings of carbon, manganese, nitrogen, and oxygen elements for the area shown in (c).

corresponding to the C–C/C–H, C–N/C═N, and C–O bond resonances, and the existence of the C–O bond indicates the abundance of oxygen functional groups on the surface of MWCNTs.[33] The N 1s spectrum, as shown in Fig. 6b, is resolved into three peaks at 398.6 eV, 399.5 eV, and 400.38 eV, confirming the formation of PANI in the PMBP composite,[34] which matches well with the peak of the C–N/C═N bond in the C 1s spectrum. The Mn 3s spectrum displays splitting due to parallel spin coupling between the 3d and 3s electrons during photoelectron ejection, as depicted in Fig. 6c. The valence of the Mn element is estimated from the following equation:

$$\Delta E \approx 7.88 - 0.85n\ (n,\ 2 \leq n \leq 4)$$

For the Mn 3s spectra, the peak-to-peak separation is 5.35 eV, indicating the 3^+ oxidation state for Mn, which is similar to those previously reported for γ-MnOOH.[35] This result is in agreement with the XRD patterns of the MBP composite. Fig. 6d shows the O 1s spectrum, which is divided into three sub-peaks that well fit the peaks of C–OH/O–C–O, Mn–OH/C═O, and Mn–O bonds. The peaks of Mn–OH and Mn–O bonds strongly demonstrate the existence of γ-MnOOH; this is in good agreement with some typical reports.[22,27]

3.2. Capacitive performance of the ternary composite

The capacitive performance of the BP, PBP, MBP, and PMBP composite electrodes was evaluated by cyclic voltammetry (CV) and galvanostatic charge/discharge (GCD) techniques in a 1 M Na_2SO_4 electrolyte solution using a three-electrode system. The CV curves of BP, PBP, MBP, and PMBP composite electrodes have been obtained at a scan rate of 5 mV s^{-1}, as shown in Fig. 7a. It is observed that the CV curve for the BP electrode has a negligible area as compared to the CV curves of the PBP, MBP, and PMBP composite electrodes. This reflects that the influence of BP's capacity is very small and thus ignorable. Among the three kinds of electrodes, PMBP shows highest specific capacitance, indicating an excellent electrochemical performance. The enhanced electrochemical performance of the ternary PMBP composite electrode originates from the combined effects of the three components. The porous structure of the free-standing BP electrode has good conductivity owing to the tight connection of the MWCNT network, which would supply a conductive path for γ-MnOOH. The γ-MnOOH nanorod array not only works as a nanostructure template to grow the PANI layer, but also provides void space to grow PANI nanorods on BP. PANI acting as a conductive path connects γ-MnOOH nanorods and BP together; this offers a special method to decrease the internal resistance of the free-standing electrode.[36] Furthermore, PANI coated on MBP offers abundant porous morphology and thus relatively large surface area, which shortens the ion diffusion paths during the charge/discharge process and sequentially enhances the electrochemical performance. As pseudocapacitive materials, the γ-MnOOH nanorods and PANI nanorods would show more excellent electrochemical

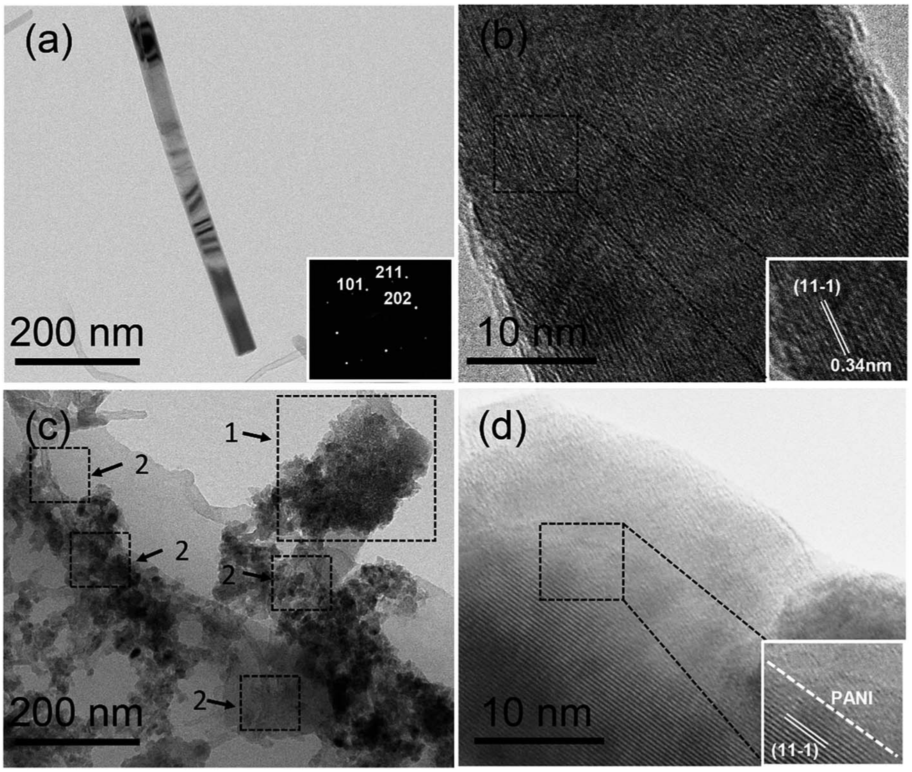

Fig. 4 (a) TEM image of the γ-MnOOH nanorod, (b) HRTEM image of the γ-MnOOH nanorod, (c) TEM image of PANI@CNTs and PANI@MnOOH, and (d) HRTEM image of the PANI@MnOOH nanostructures. The inset in (a) shows the FFT image, and the insets in (b & d) show the enlarged images of respective nanostructures.

performance than the binary nanorods; this indicates the positive synergistic effect of γ-MnOOH and PANI. Fig. 7b shows the CV curves of the PMBP composite electrode at different scan rates. The cathodic peaks shift towards positive potential and the anodic peaks shift towards negative potential with the increase of potential scan rates from 1 mV s^{-1} to 20 mV s^{-1}. The more detailed CV curves of γ-MnOOH and PANI are shown in Fig. S4.† The areas of the CV curves for the binary composite electrodes (MBP and PBP) are larger than those for the corresponding components at the scan rate of 5 mV s^{-1}; this indicates that the PMBP composite electrode has largest specific capacitance among all electrodes.

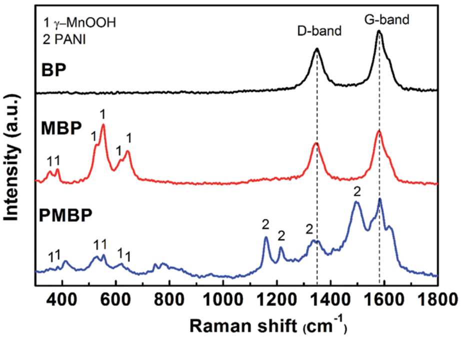

Fig. 5 Raman spectra of BP, MBP, and PMBP.

Fig. 8a shows the GCD measurements that were performed for the PBP, MBP, and PMBP composite electrodes. Fig. 8a depicts the comparison between the GCD curves of PBP, MBP, and PMBP composite electrodes at the current density of 0.8 A g^{-1}, which indicates that PMBP exhibits a good electrochemical performance. The specific capacitance was calculated using the following equation:

$$C_g = (I \times \Delta t)/(V \times m)$$

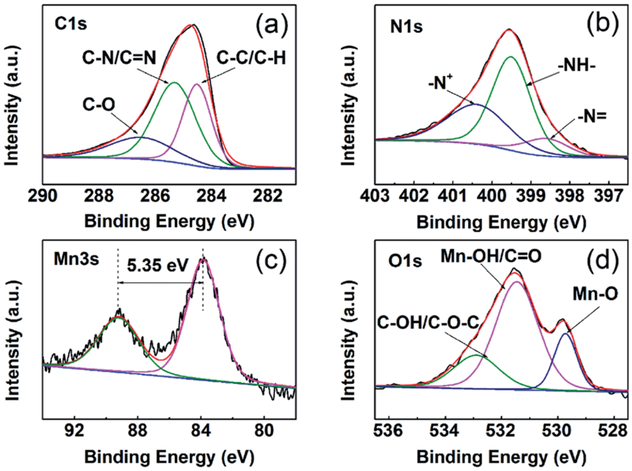

Fig. 6 XPS spectra of (a) C 1s, (b) N 1s, (c) Mn 3s, and (d) O 1s for PMBP.

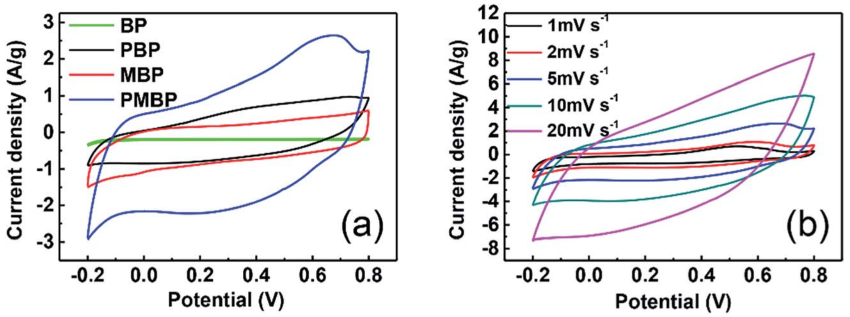

Fig. 7 CV curves of (a) BP, PBP, MBP, and PMBP at a scan rate of 5 mV s^{-1}, and (b) PMBP at scan rates of 1, 2, 5, 10, and 20 mV s^{-1}.

where C_g, I, t, V, and m represent the specific capacitance (F g^{-1}), the discharge current (A), the discharge time (s), potential window (V), and the mass of active materials (g), respectively. Fig. 8b depicts the capacitance performances of PBP, MBP, and PMBP electrodes. It is evident from the whole range of current densities that the ternary electrode has higher specific capacitance than the binary electrodes. The PBMP electrode exhibits the highest specific capacitance of 480.7 F g^{-1} as compared to the PBP electrode (205.7 F g^{-1}) and the MBP electrode (234.2 F g^{-1}) at a current density of 0.8 A g^{-1}. Specially, PMBP and PBP electrodes still deliver high capacitances of 567.5 F g^{-1} and 250 F g^{-1}, respectively, at the current density of 0.5 A g^{-1}. However, the specific capacitance of the MBP electrode cannot be measured because it cannot be charged to 0.8 V at the same current density.

Based on the calculation results, the ternary composite electrode shows a much higher specific capacitance than the other binary composite electrodes; this indicates that PMBP displays the best performance owing to the good conductivity of the PANI nanorod network and coverage of PANI on γ-MnOOH and BP.

Fig. 8c represents the GCD curves of the PMBP electrode at different current densities ranging from 0.5 A g^{-1} to 4 A g^{-1} (or from ≈0.27 mA cm^{-2} to 2.12 mA cm^{-2}). The GCD curves of the PMBP electrode show a slight bend, which results from the pseudocapacitive effect. The areal capacitance was calculated using the following equation:

$$C_s = (I \times \Delta t)/(V \times s)$$

where the C_s, I, t, V, and s are the areal capacitance (mF cm^{-2}), the discharge current (A), the discharge time (s), potential window (V), and the area of active materials (cm^2), respectively. The PMBP composite electrode retains a high areal capacitance of 172.6 mF cm^{-2} at a high current density of 2.12 mA cm^{-2}. The charge/discharge process took a longer time at low current density due to the sufficient intercalation and deintercalation of Na$^+$ ions at the PMBP electrode during the charge/discharge

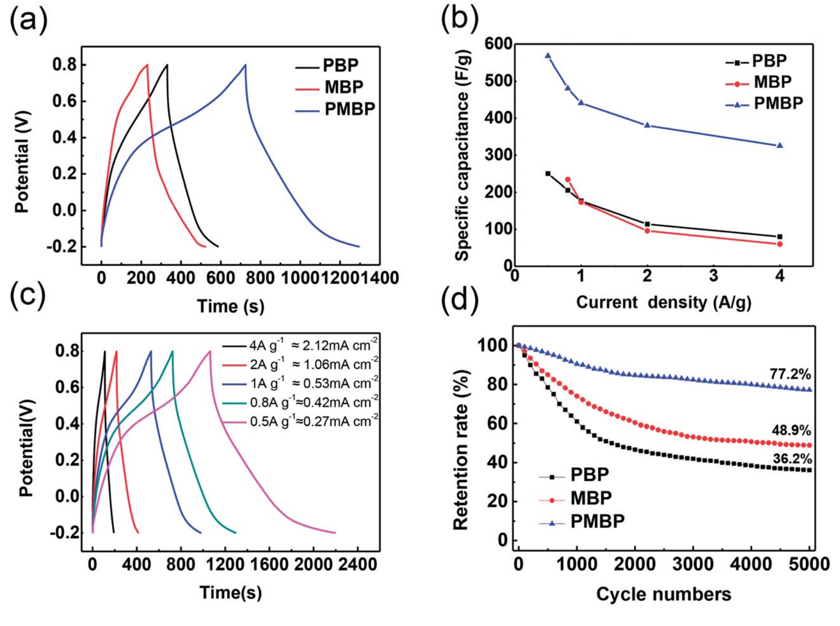

Fig. 8 (a) CD curves of PBP, MBP, and PMBP at the current density of 0.8 A g^{-1}. (b) The specific capacitances of PBP, MBP, and PMBP composites at different current densities. (c) CD curves of PMBP at different current densities. (d) Retention rates changing with cycle number at 4 A g^{-1} for PBP, MBP, and PMBP.

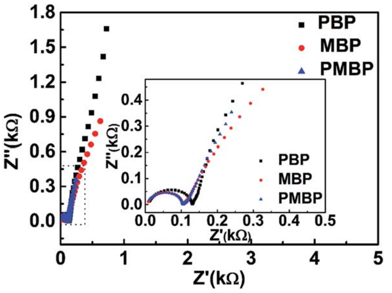

Fig. 9 Nyquist impedance plots of PBP, MBP, and PMBP electrodes.

process. With an increase in current density from 1.06 to 0.27 mA cm^{-2}, the PMBP composite electrode reaches relatively high areal capacitive values of 202.7, 242.6, 255.1, and 301.2 mF cm^{-2}. The cyclic stability of the PMBP, MBP, and PBP composite electrodes was measured through GCD at a current density of 4 A g^{-1} for 5000 cycles, as illustrated in Fig. 8d. It is observed that the specific capacitance of the PMBP composite electrode decreases slowly, and it retains 77.2% of its initial specific capacitance after 5000 cycles, higher than those of the PBP composite electrode (36.2%) and MBP composite electrode (48.9%); this indicates its best stability among the three kinds of electrodes.

To explain the best electrochemical performance of the PMBP composite electrode among the three kinds of electrodes, electrochemical impedance spectroscopy (EIS) was employed, as shown in Fig. 9. The EIS analysis of PBP, MBP, and PMBP composite electrodes was performed in the frequency range from 0.1 Hz to 100 KHz at the open circuit potential with an AC perturbation of 5 mV. All the Nyquist plots show the semicircles in the high frequency region, which is related to the combined resistance (R_s) and the charge transfer resistance (R_{ct}). The PMBP and MBP nanocomposite electrodes show less R_{ct} than the PBP composite; this indicates that the γ-MnOOH nanorod array plays an important role in decreasing the resistance between the electrode and solution interfaces and supplies the 3D structure for a more accessible area for sufficient intercalation and deintercalation during the charge/discharge processes. In the low frequency range, the Nyquist plots are relatively vertical, and the PMBP and PBP nanocomposite electrodes are more suitable for fast electrolyte ion diffusion than MBP; this indicates that the porous structure of PANI on the surface of the electrode improves the ability of ion diffusion. The lower R_{ct} and the faster ion diffusion of the PMBP composite electrode indicate the best electrochemical performance; this is in agreement with the results analyzed form the CV and GCD curves.

4. Conclusion

A uniform PANI@γ-MnOOH–BP ternary composite was synthesized through a facile two-step process. The ternary freestanding PMBP composite electrode exhibited a high specific capacitance of 567.5 F g^{-1} at a current density of 0.5 A g^{-1} or an areal capacitance of 301.2 mF cm^{-2} at a current density of 0.27 mA cm^{-2} in a 1 M Na_2SO_4 aqueous solution and good cyclic stability by retaining 77.2% specific capacitance after 5000 cycles. Morphological and structural characterization reveal the growth of PANI, which are either intercalated into the γ-MnOOH nanoparticles or cover the surface of γ-MnOOH nanorods. This enhances the intercalation/deintercalation of ions on the surface of the PMBP electrode and inter-bridge γ-MnOOH and PANI. Moreover, the high conductivity of BP improves the electron transfer process and enhances the mechanical stability of the active material (γ-MnOOH@PANI) acting as a freestanding electrode. The abovementioned results show that the synthesized hierarchical nanostructures can be used as a potential candidate for free-standing high-performance electrode materials for SCs.

Conflicts of interest

There are no conflicts to declare.

Acknowledgements

This work was financially supported by the National Natural Science Foundation of China (No. 51661145025, 11274055, 61520106013).

References

1 Y. L. Shao, M. F. El-Kady, C. W. Lin, G. Z. Zhu, K. L. Marsh, J. Y. Hwang, Q. H. Zhang, Y. G. Li, H. Z. Wang and R. B. Kaner, *Adv. Mater.*, 2016, **28**, 6719–6726.
2 S. Y. Gan, L. J. Zhong, T. S. Wu, D. X. Han, J. D. Zhang, J. Ulstrup, Q. J. Chi and L. Niu, *Adv. Mater.*, 2012, **24**, 3958–3964.
3 X. W. Yang, C. Cheng, Y. F. Wang, L. Qiu and D. Li, *Science*, 2013, **341**, 534–537.
4 J. B. Wu, X. Gao, H. M. Yu, T. P. Ding, Y. X. Yan, B. Yao, X. Yao, D. C. Chen, M. L. Liu and L. Huang, *Adv. Funct. Mater.*, 2016, **26**, 6114–6120.
5 J. Pu, X. H. Wang, R. X. Xu and K. Komvopoulos, *ACS Nano*, 2016, **10**, 9306–9315.
6 Y. Jin, H. Y. Chen, M. H. Chen, N. Liu and Q. W. Li, *ACS Appl. Mater. Interfaces*, 2013, **5**, 3408–3416.
7 Z. Niu, W. Zhou, J. Chen, G. Feng, H. Li, W. Ma, J. Li, H. Dong, Y. Ren and D. Zhao, *Energy Environ. Sci.*, 2011, **4**, 1440–1446.
8 W. Liu, M. S. Song, B. Kong and Y. Cui, *Adv. Mater.*, 2016, **29**, 1603436.
9 M. D. Stoller, S. J. Park, Y. W. Zhu, J. H. An and R. S. Ruoff, *Nano Lett.*, 2008, **8**, 3498–3502.
10 Y. L. Shao, M. F. El-Kady, L. J. Wang, Q. H. Zhang, Y. G. Li, H. Z. Wang, M. F. Mousavi and R. B. Kaner, *Chem. Soc. Rev.*, 2015, **44**, 3639–3665.
11 R. Raccichini, A. Varzi, S. Passerini and B. Scrosati, *Nat. Mater.*, 2015, **14**, 271–279.
12 Y. X. Xu, G. Q. Shi and X. F. Duan, *Acc. Chem. Res.*, 2015, **48**, 1666–1675.
13 M. Wang, X. D. Duan, Y. X. Xu and X. F. Duan, *ACS Nano*, 2016, **10**, 7231–7247.

14 S. H. Yang, X. F. Song, P. Zhang and L. Gao, *J. Mater. Chem. A*, 2015, **3**, 6136–6145.

15 S. M. Sun, S. Wang, T. C. Xia, X. F. Li, Q. X. Jin, Q. Wu, L. Z. Wang, Z. H. Wei and P. Y. Wang, *J. Mater. Chem. A*, 2015, **3**, 20944–20951.

16 M. Toupin, T. Brousse and D. Bélanger, *Chem. Mater.*, 2004, **16**, 3184–3190.

17 H. T. Tan, X. Rui, W. Shi, C. Xu, H. Yu, H. E. Hoster and Q. Yan, *ChemPlusChem*, 2013, **78**, 554–560.

18 Z. C. Li, H. L. Bao, X. Y. Miao and X. H. Chen, *J. Colloid Interface Sci.*, 2011, **357**, 286–291.

19 H. Fang, S. C. Zhang, X. M. Wu, W. B. Liu, B. H. Wen, Z. J. Du and T. Jiang, *J. Power Sources*, 2013, **235**, 95–104.

20 C. Sha, B. Lu, H. Mao, J. Cheng, X. Pan, J. Lu and Z. Ye, *Carbon*, 2016, **99**, 26–34.

21 Q. Li, J. Liu, J. Zou, A. Chunder, Y. Chen and L. Zhai, *J. Power Sources*, 2011, **196**, 565–572.

22 C. Pan, H. Gu and L. Dong, *J. Power Sources*, 2016, **303**, 175–181.

23 J. Han, L. Li, P. Fang and R. Guo, *J. Phys. Chem. C*, 2012, **116**, 15900–15907.

24 H. L. Li, Y. He, V. Pavlinek, Q. L. Cheng, P. Saha and C. Z. Li, *J. Mater. Chem. A*, 2015, **3**, 17165–17171.

25 G. Han, Y. Liu, L. Zhang, E. Kan, S. Zhang, J. Tang and W. Tang, *Sci. Rep.*, 2014, **4**, 4824.

26 H. Jiang, J. Ma and C. Z. Li, *J. Mater. Chem.*, 2012, **22**, 16939–16942.

27 T. Gao, F. Krumeich, R. Nesper, H. Fjellvag and P. Norby, *Inorg. Chem.*, 2009, **48**, 6242–6250.

28 Y. C. Zhang, T. Qiao, X. Y. Hu and W. D. Zhou, *J. Cryst. Growth*, 2005, **280**, 652–657.

29 T. Kohler, T. Armbruster and E. Libowitzky, *J. Solid State Chem.*, 1997, **133**, 486–500.

30 X. Fu, Y. M. Sun, N. Zhou, L. J. Pan, M. Usman, Z. M. Gao, X. N. Wang, Y. Y. Huang, J. Qin and M. Asif, *Electrochim. Acta*, 2016, **210**, 111–116.

31 M. C. Bernard, A. H. L. Goff, B. V. Thi and S. C. Detorresi, *J. Electrochem. Soc.*, 1993, **140**, 3065–3070.

32 R. V. Salvatierra, M. M. Oliveira and A. J. G. Zarbin, *Chem. Mater.*, 2010, **22**, 5222–5234.

33 M. Asif, Y. Tan, L. J. Pan, M. Rashad, J. Y. Li, X. Fu and R. X. Cui, *Phys. Chem. Chem. Phys.*, 2016, **18**, 26854–26864.

34 O. C. Compton and S. T. Nguyen, *Small*, 2010, **6**, 711–723.

35 V. Khomenko, E. Raymundo-Piñero and F. Béguin, *J. Power Sources*, 2010, **195**, 4234–4241.

36 M. Usman, L. J. Pan, M. Asif and Z. Mahmood, *J. Mater. Res.*, 2015, **30**, 3192–3200.